Real-Time Ultra-Wideband Channel Sounder Design for 3-18 GHz

C. Umit Bas, *Student Member, IEEE*, Vinod Kristem,
Rui Wang, *Student Member, IEEE*, Andreas F. Molisch, *Fellow, IEEE*

***Abstract*—This paper presents system design, calibration and example measurements of a novel ultra-wideband, low-cost, real-time channel sounder. The channel sounder operates in the frequency range from 3 GHz to 18 GHz with a 15 GHz bandwidth thus providing a Fourier delay resolution of 66.7 ps. It sequentially measures overlapping sub-bands of 1 GHz bandwidth to cover the whole frequency range. By using a waveform generator and a digitizer with relatively lower sample rates, the design significantly lowers the cost compared to sampling the whole band simultaneously. With the transmitting power of 40 dBm, the maximum measurable path loss is 132 dB without accounting for possible antenna gains. In this work, we also describe the calibration procedure along with the method to stitch sub-bands into a combined channel response across 15 GHz of bandwidth. The channel sounder performance is compared with vector network analyzer (VNA) measurements acquired in the same static channels. In contrast to VNAs, however, our channel sounder can measure the whole band in 6 ms and can thus operate in dynamic environments with coherence time more than 6 ms. Additionally, we present sample results from a measurement campaign performed in an indoor corridor investigating the delay spreads statistics over the range of 3-18 GHz.**

I. Introduction

As the number of applications (virtual reality, augmented reality, etc.) and their bandwidth requirements for wireless communications increase, the need for frequency spectrum has also grown [2]. Since the frequencies lower than 6 GHz are mostly occupied, this need can only be met by utilizing the ample spectrum at the higher frequencies that is currently lying fallow or under-utilized. In particular, the emergence of fifth generation (5G) cellular communications has significantly increased interest in millimeter-wave (mmWave) communications and motivated propagation channel measurements at higher frequencies [3]–[5].

Although there has been increasing interest in the bands between 6 GHz and 20 GHz [6], most of the measurement campaigns performed so far focus on bands below 6 GHz [7]–[11] or above 20 GHz [12]–[18]. It is commonly accepted that the new mmWave systems will have to coexist with the legacy networks (4G, LTE, WiFi, etc.) operating mostly below 6 GHz. Consequently, a host of other papers [19]–[24] compared the characteristics of below 6 GHz channels with mmWave propagation and discuss the frequency dependency of the channel parameters. However, all of these works measure disjoint sub-bands rather than a continuous frequency range. Furthermore, except [20]–[22], the measurements at the different carrier frequencies are not performed with the same setup (i.e., either separate up- and down-conversion chains for each frequency or completely isolated channel sounders). Consequently, comparisons of parameters such as delay spread are difficult due to varying dynamic range of the receivers.

Another type of wideband system that has drawn interest is ultra-wideband (UWB) communications which operate from 3.1 GHz to 10.6 GHz. UWB channels have been well investigated for indoor, outdoor or vehicular scenarios, e.g., [25]–[27]. Most of these measurements were performed with vector network analyzers (VNAs), which can only operate in static environments, or with time domain channel sounders requiring costly pieces of equipment such as high-speed (more than 10 GSps) arbitrary waveform generators (AWGs) and digitizers [28]. Hence it is neither practical nor cost-efficient to expand these setups beyond 10 GHz.

To fill this gap, we designed a channel sounder that can perform measurements over the continuous band from 3 GHz to 18 GHz by utilizing a hybrid time/frequency domain approach. Even though the instantaneous bandwidth of the setup is only 1 GHz (thus allowing the use of relatively lower-cost components compared to the direct sampling approach which requires 40 GSps AWG and digitizer), by utilizing a sweeping sub-band approach, it can measure up to 15 GHz total bandwidth within 6 ms. The short measurement time allows to measure in dynamic environments as long as the coherence time of the channel is more than 6 ms. At 18 GHz this would correspond to a maximum speed of 5 km/h, which is the typical pedestrian speed [29]. Since the measurement time for our setup is directly proportional to the total bandwidth, measurements in more mobile environments can be performed with a smaller bandwidth. In comparison, a VNA, which is the standard choice of equipment for such large bandwidth measurements, would require much longer time for similar measurements. For example, for a Keysight programmable VNA (PNA) 5224B, for the same frequency range (3-18 GHz) and with the same number of frequency points (30001) and 600 kHz intermediate frequency bandwidth (similar to our frequency spacing of 500 kHz), the minimum sweep time is 72 ms compared to the 6 ms for our channel sounder. The frequency resolution (subcarrier spacing) in our channel sounder is 500 kHz,

C. U. Bas, V. Kristem, R. Wang and A.F. Molisch are with the Department of Electrical Engineering, University of Southern California (USC), Los Angeles, CA 90089-2560 USA.

Part of this work was presented in IEEE Military Communications Conference 2017 [1].

Part of this work was supported by the National Science Foundation under projects ECCS-1126732 and CIF-1618078, and by Northrop Grumman under a DARPA subcontract.

corresponding to a maximum measurable excess run-length of multi-path components (MPCs) of 600 m (2 μs pseudorange), which is sufficient even for most outdoor measurements. Additionally, unlike a VNA, the transmitter (TX) and the receiver (RX) in our setup are physically separated, and they do not require any cable connections since the synchronization is provided by Global Positioning System (GPS)-stabilized Rubidium frequency references. Hence, the channel sounder can operate in almost any desired measurement environment with a coherence time more than 6 ms. Consequently, the channel sounder is used for outdoor cellular measurements [30], [31] and the indoor measurement campaign discussed in this paper.

There has been limited work utilizing a sub-band or multi-band measurement approach. In [32], a similar approach is used to perform measurements at 60 GHz. However the total measurement time in the proposed setup is 10 s for 5 GHz of total bandwidth so that (contrary to our setup) the channel sounder in [32] can only be used in static scenarios. Furthermore, the frequency resolution achieved was 8 MHz limiting the maximum measurable delay spread to 37.5 m. Similarly, the channel sounder proposed in [33] uses a narrow band system to perform wide band measurements with a total 1 GHz bandwidth. Another channel sounder with the multi-band approach was presented in [34]. The channel sounder in [34] utilizes software defined radios and measures 10 sub-bands of 20 MHz providing a total bandwidth of 200 MHz around 5.6 GHz in 3 ms. While this enables measurements in dynamic environments, the bandwidth is almost two orders of magnitude lower than that in our setup. Furthermore, in both of the previous works, the TX and the RX units require a cable connection for sharing reference signals and control signals. Consequently, neither of the setups are suitable for long range measurements. In addition, the enormous bandwidth of our designed channel sounder introduces additional challenges such as frequency dependent IQ imbalance and system gain. The frequency dependencies necessitate additional steps to be taken during the operation of the channel sounder and the post processing of the data, see Sections II and III.

The contributions of this work include:

- Designing a low-cost hybrid time/frequency domain channel sounder setup with a total bandwidth of 15 GHz in 6 ms measurement time,
- Describing the method for channel sounder calibration to overcome hardware imperfections in setups,
- Proposing a method to concatenate multiple sub-bands into a wide-band frequency response,
- Presenting validation measurements and investigating channel sounder performance,
- Showing sample results for the frequency dependency of the root mean square delay spread (RMS-DS) in an indoor channel sounding campaign with the proposed setup.

This paper is organized as follows. Section II describes the details of the channel sounder setup and its operation principles. Section III discusses the channel sounder calibration steps and Section IV demonstrates performance evaluations for the setup. Section V describes the measurement environment for the channel sounding campaign along with the detailed post-processing steps and the results. Finally, Section VI concludes the paper with a summary and discussion of future work.

II. Channel Sounder Design

The proposed setup is a real-time, frequency-hopped multi-band channel sounder with direct up/down-conversion. The TX and the RX were built as physically separate structures and they do not require any cable connection, allowing arbitrary placement of the TX and the RX. Figs. 1 and 2 show the block diagrams for the TX and the RX respectively. Furthermore, Table I lists the part numbers and descriptions of all the units used in the setup.

A. Single Band Measurements

The TX operation for a single band measurement can be summarized as follows. A 15-bit, 1.25-GSps AWG generates the complex baseband sounding signal. In this measurement campaign, the sounding signal is a multi-tone waveform represented as:

$$m(t) = \sum_{n=-N}^{N} e^{j(n2\pi\Delta f t + \theta_n)} \tag{1}$$

where Δf is the tone spacing, $2N+1$ is the number of tones and θ_n is the phase of the tone n. In order to find the phases of a multi-tone signal that minimizes the peak to average power ratio (PAPR), we implemented an iterative algorithm that attempts to reduce the high peaks in the time-domain waveform $m(t)$ [35]. The algorithm switches between the time and the frequency domain representation of the waveforms. In each iteration step, the error signal is computed by cropping the parts of $m(t)$ whose amplitudes are larger than a certain threshold. The removal of these high peaks is performed in the frequency domain by subtracting the frequency coefficients of the error signal from the current frequency coefficients. The new frequency coefficients are normalized to maintain the flat-top multi-tone waveform (i.e., the magnitude of each frequency coefficient is 1). Then, the updated $m(t)$ is calculated from new frequency coefficients. The algorithm iterates until the PAPR drops below a predetermined threshold. Note that the waveform can be precomputed off-line, and then is just stored in the AWG. In our case the PAPR was 0.4 dB, allowing us to transmit with power as close as possible to the 1 dB compression point of the power amplifier without driving it into saturation. The in-phase and quadrature (I and Q) components of the signal are the real and imaginary parts of $m(t)$ respectively. The 500 MHz I and Q signals are generated by 2 channels of the AWG and transmitted to an IQ mixer via phase-matched cables. The IQ mixer directly up-converts the baseband I and Q signals to a 1 GHz radio frequency (RF) signal around the carrier frequency provided by the frequency synthesizer. Finally, the RF signal is amplified and transmitted by a biconical antenna with a frequency range of 1 GHz to 18 GHz. Figs. 3(a) and 3(b) show the azimuth and elevation patterns of the antenna measured in an anechoic chamber.

TABLE I
LIST OF THE UNITS SHOWN IN FIGS. 1 AND 2 ALONG WITH THEIR DESCRIPTIONS AND RELEVANT SPECIFICATIONS

Unit Number	Unit Name	Unit Description
(1)	Agilent N8241A	2-channel AWG, 15-bit resolution, 1.25-GSps sample rate
(2)	MLIQ-0218I	IQ Mixer, 8.5 dB conversion loss
(3)	RHPF23G03G18	High pass filter, 2.1 dB insertion loss, 3-18 GHz pass band
(4)	GT1000B	Power amplifier, 40 dBm output power
(5)	SAS-547	Biconical antenna, 1-18 GHz frequency range
(6)	PAM-118A	Low noise amplifier, 3 dB noise figure, 40 dB gain
(7)	National Instruments PXIe-5160	2-channel ADC, 10-bit resolution, 1.25-GSps sample rate
(8)	National Instruments HDD-8265	Raid array, 6 TB capacity, 700 MBps read/write speed
(9)	Phase Matrix FSW-0020	Frequncy synthesizer, 0.2-20 GHz frequency range
(10)	Precision Test Systems GPS10eR	GPS-disciplined Rubidium Reference, Allan Deviation(1s) $<$ 1.5e-12
(11)	National Instruments PXIe-8135	2.3 GHz Quad-Core PXI Controller
(12)	National Instruments PXIe-6361	Multifunction I/O Module, 32-bit counters at 100 MHz clock
(13)	National Instruments PXIe-1082	PXIe Chassis

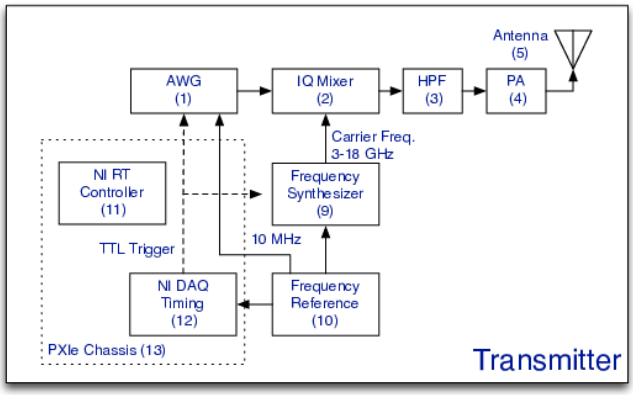

Fig. 1. Transmitter block diagram, the descriptions of the units are given in Table I

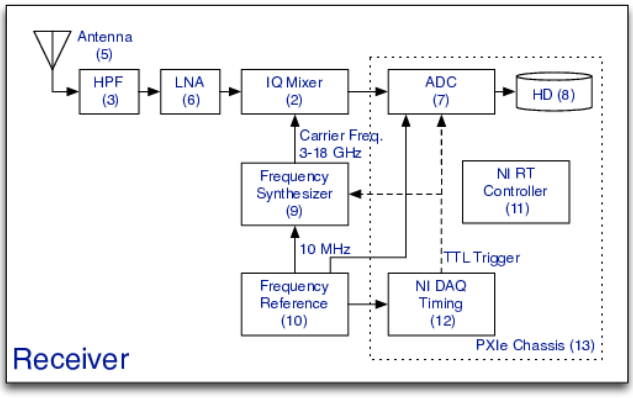

Fig. 2. Receiver block diagram, the descriptions of the units are given in Table I

The RX operates in a similar manner to the TX. The received RF signal is fed through a high pass filter (HPF) to eliminate any out-of-band interference from below 3 GHz band. Then the filtered signal is amplified by the low noise amplifier (LNA) and down-converted to baseband I/Q signals by the IQ mixer. The baseband I/Q signals are sampled with a 10-bit, 2-channel analog to digital converter (ADC). The acquired data is streamed into a 6 terabyte (TB) redundant array of independent disks (RAID), which is equipped with a

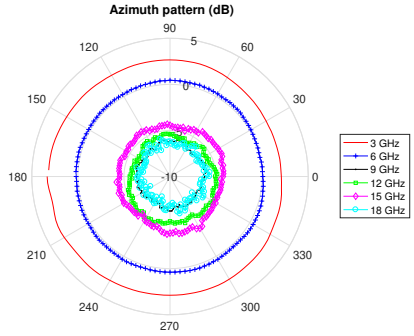

(a) Azimuth pattern in dB

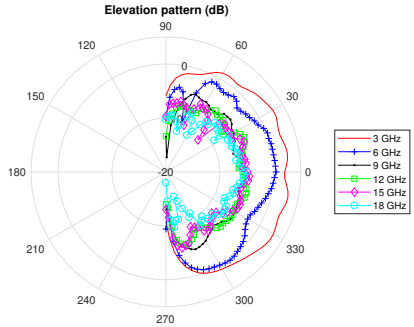

(b) Elevation pattern in dB

Fig. 3. Measured azimuth and elevation patterns of the biconical antenna for frequencies between 3-18 GHz

PCIe x4 connection allowing 700 MBps sustained data write speed. With the fast streaming capability and the 6 TB of data storage, the channel sounder can perform measurements for more than 2 hours with a 40% duty cycle (i.e 40% of the time, the channel sounder performs measurements and in parallel, continuously streaming the acquired data to the RAID array). With the current configuration the 10-bit ADC generates 2-Bytes per sample. The duty cycle can be doubled by limiting the ADC to 8-bit per sample, if necessary. We also note that this is an important difference to the use of a sampling oscilloscope at the RX. While a suitable scope could easily receive the whole 15 GHz bandwidth of interest, it could not provide the sustained reading/writing required, e.g., for measuring the channel evolution as the mobile station moves on a trajectory.

Fig. 4. Operation of the timing module to trigger AWG (TX) or ADC (RX) and frequency synthesizers

Both the TX and the RX are controlled with Labview scripts running on National Instruments (NI) real-time controllers. The TX and the RX operations are synchronized by using hardware counters in NI DAQ timing modules, see Section II-B for further details. GPS-stabilized Rubidium frequency references provide two signals for the timing of the setup; a 10 MHz clock to be used as a timebase for all units and 1 pulse per second (PPS) signal aligned to Coordinated Universal Time (UTC). Since the 1 PPS signals in the TX and the RX are both aligned to the UTC, they operate synchronously without requiring any physical connections. More importantly, the AWG, the ADC, and the frequency synthesizers are disciplined with the 10 MHz signal provided by these frequency references, thereby maintaining phase stability during the measurements, which is essential for the accurate measurement results [36]. The frequency references also provide GPS locations, which are logged along with the measurement data.

B. Multi Band Measurements

All RF units mentioned in Section II-A can operate from 3 GHz to 18 GHz. Additionally, the frequency synthesizers can switch between two arbitrary frequencies within this range in less than 100 μs. Hence they can change the carrier frequency every 100 μs, which is the main feature which allows the construction of the real-time channel sounder with a frequency sweep approach. One can think of the proposed channel sounder as a hybrid design lying between a VNA and a time-domain channel sounder setup. Similar to a VNA, it sweeps through different frequency tones to obtain the frequency response of the channel under investigation. However, unlike a VNA using a single tone at a time, it uses a wide-band signal that itself consists of 2001 simultaneously transmitted tones.

The first algorithm describes the operation for the multi-band measurements; the same procedure runs in the TX and the RX in parallel. In summary, we perform 30 channel measurements each with 1 GHz bandwidth and center frequencies of 3.25 GHz to 17.75 GHz with 500 MHz spacing. Given the measurement period and the duration to measure each sub-band, hardware counters in the NI DAQ timing modules count the rising edges of the 10 MHz clock and generate the trigger waveforms for the frequency synthesizer (to switch to the next carrier frequency) as well as the AWG at the TX and the ADC at the RX. Fig. 4 depicts the counter operation for the counter values corresponding to the 200 μs per band measurement duration and 6 ms total sweep time. To allow the frequency synthesizers to be stabilized, both the AWG and ADC wait for 120 μs once they received the trigger and then operate for 80 μs, which consists of 20 repetitions of the sounding waveform. Furthermore, since both the TX and the RX counters start with the 1 PPS signals provided by the frequency references, the triggers at the TX and the RX are well-aligned. The NI DAQ timing module has an internal base clock of 100 MHz, which limits the maximum offset between the TX and the RX to less than 10 ns. This process is repeated for all sub-bands and the acquired data and the metadata (including GPS location, time, ADC gain, etc.) are transferred from the field programmable gate array (FPGA) of the RX into the permanent storage in 1-second chunks.

Algorithm 1 Multi-band Operation: N_{m}, N_{bands} and N_{sweeps} are the measurement duration in seconds, number of sub-bands to be measured, and repetition of multi-band measurements per second respectively.

procedure SWEEP SOUNDER(N_{m},N_{bands},N_{sweeps})
  $i \leftarrow 0$
  while $i < N_{\mathrm{m}}$ **do**
    while 1 PPS trigger not received **do**
      Wait
    end while
    Start counter for sub-band trigger
    for $k = 0$, $k{+}{+}$, $k < N_{\mathrm{bands}} \times N_{\mathrm{sweeps}}$ **do**
      $l \leftarrow k$ *mod* N_{bands}
      $s \leftarrow k$ *div* N_{bands}
      while sub-band trigger not received **do**
        Wait
      end while
      Wait for 120μs
      Channel sounding for sub-band l in sweep s
    end for
    Store the data
    Log GPS location and time
    Stop counter
    $i \leftarrow i + 1$
  end while
end procedure

Since the frequency synthesizer is basically a phase locked loop (PLL), every time it switches into a new carrier frequency it introduces a random phase offset relative to the previous carrier. Moreover, the triggering uncertainties of the AWG and ADC add additional phase offsets between the TX and the RX. The phase offsets can be estimated and corrected if two adjacent sub-bands have overlapping frequency tones. Thus, the frequency plan for the multi-band measurements is designed accordingly as shown in Fig. 5. More details about phase correction are given in Section III-B. One of the main motivations of this setup was to investigate the frequency dependency of the channel statistics. Hence for a fair comparison, we ensured a similar dynamic range through-out

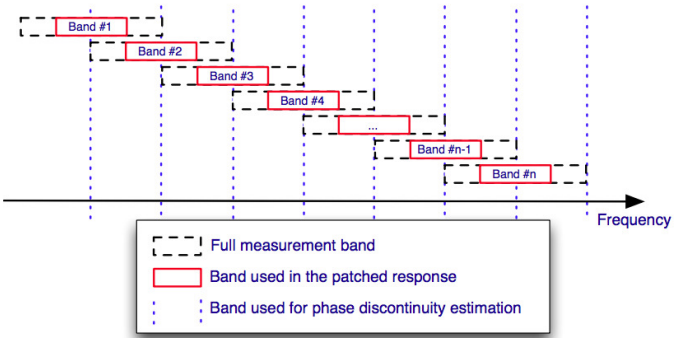

Fig. 5. The frequency plan for the multi-band measurements, overlap of the adjacent sub-bands are used to estimate the discontinuities of the frequency and phase responses.

TABLE II
CHANNEL SOUNDER SPECIFICATIONS, PROVIDING THE VALUES USED THROUGHOUT THE PAPER. NOTE, HOWEVER, THAT THE VALUES CAN BE MODIFIED ON A PER-CAMPAIGN BASIS.

Hardware Specifications	
Frequency range	3-18 GHz
Instantaneous bandwidth	1 GHz
Carrier spacing	500 MHz
Frequency switching speed	100 μs
TX power	40 dBm
RX noise figure	$\leq$ 5 dB
ADC/AWG resolution	10/15-bit
Data streaming speed	700MBps
Sounding Waveform Specifications	
Waveform duration	2 μs
Repetition per band	20
Number of tones per band	2001
Tone spacing	500 kHz
PAPR	0.4 dB
Total sweep time	6 ms
Total number of tones	30001
Delay resolution	66.667 ps (2 cm)
Max delay spread	2 μs

the whole frequency range. To achieve this, the transmitting signal was pre-distorted to compensate the gain of the system response on a per band basis. The final dynamic range only varies ± 1.5 dB due to the variations of the RX noise figure caused by the LNA noise figure.

Table II summarizes the configuration of the channel sounder for the measurements presented in this work. The full sweep consists of 30001 tones with 500 kHz spacing over 15 GHz total bandwidth. This configuration provides a time resolution of 66.67 ps with a maximum measurable delay spread of 2 μs. Hence the channel sounder is capable of distinguishing two MPCs, if their run-lengths differ by more than 2 cm, and it can measure up to 600 m of maximum run-length for MPCs. However, thanks to the flexible design, almost all the parameters given in the table can be modified according to the goal of the particular channel sounding campaign. For example, the channel sounder can operate as low as 2 GHz. However, due to interference from WLAN and cellular networks, and the presence of licensed spectrum bands we limited our measurements to 3-18 GHz during this campaign. Note that with the addition of band-pass filters, the channel sounder can also operate like a generic time-domain channel sounder setup with 1 GHz bandwidth and a carrier frequency anywhere between 2 to 18 GHz without any modifications.

III. CALIBRATION

A. Sub-band Estimation

The frequency response of each sub-band k is estimated with a least squares approach as follows:

$$\hat{H}_k(f_t) = \frac{(H_{\mathrm{m},k}(f_t)/H_{\mathrm{cal},k}(f_t))}{E_\phi\{H_{\mathrm{ant},k}(f_t,\phi)\}} \tag{2}$$

where $H_{\mathrm{m},k}(f)$ and $H_{\mathrm{cal},k}(f)$ are the measured channel response and system response for the k-th sub-band, respectively. $H_{\mathrm{ant},k}(f,\phi)$ is the antenna response for the k-th sub-band at the azimuth angle $\phi \in [0, 2\pi)$. $E_\phi\{\cdot\}$ is the mean taken over ϕ to average out the variations in the azimuth pattern. The system response, $H_{\mathrm{cal},k}(f)$, is measured with a thru connection (i.e., by connecting TX and RX RF ports directly) prior to the each measurement campaign. The least squares estimation is only performed on the tone frequencies, i.e., $f_t \in [f_{\mathrm{LO}} - 500\ \mathrm{MHz}, f_{\mathrm{LO}} + 500\ \mathrm{MHz}]$. Since each f_t in the given frequency tone is occupied with a sounding tone and the calibration response $H_{\mathrm{cal},k}(f)$ and the antenna response $H_{\mathrm{ant},k}(f,\phi)$ are measured with signal to noise ratios (SNRs) better than 40 dB, the noise enhancement in the least squares estimation is not an issue. Even though the biconical antennas have a nominally omnidirectional pattern, there are some deviations from that ideal behavior, see Fig. 3(a). Thus, the measured frequency responses of antennas are averaged over all azimuth angles for single-antenna measurements, such as the ones presented here (for directional measurements, obtained, e.g., with an array, the actual directional patterns would be taken into account in the calibration and evaluation).

Since the proposed setup utilizes zero-IF up- and down-conversion, there are two main imperfections of the IQ mixers that need to be dealt with; local oscillator (LO) leakage and IQ phase/amplitude imbalance. For the down-conversion mixer (RX side), the LO leakage is filtered out by the low pass filter of the ADC and does not affect the measurements. Conversely, in the up-conversion (TX side), if LO power is not properly managed, LO leakage might drive the power amplifier into saturation since the leaked LO will be in the same frequency range as the up-converted RF signal. Consequently, LO power and the power of the baseband sounding signal are adjusted on a per-band basis to ensure that the up-converted RF signal has always more power than the LO leakage and the total power is at least 2 dB less than the input 1 dB compression point of the power amplifier. At the RX end, the tones located in $[f_{\mathrm{LO}} - 2\Delta f, f_{\mathrm{LO}} + 2\Delta f]$ are simply ignored to avoid any misinterpretations due to LO leakage of the IQ mixers.

The imbalances between I and Q channels are measured separately for the TX and the RX with the method suggested in [37] prior to the measurement campaigns. For both mixers, the deviation of the relative phase between I and Q channels from 90 degrees, and the mismatch in the amplitudes, are estimated on a per sub-band base. Then for all measurements,

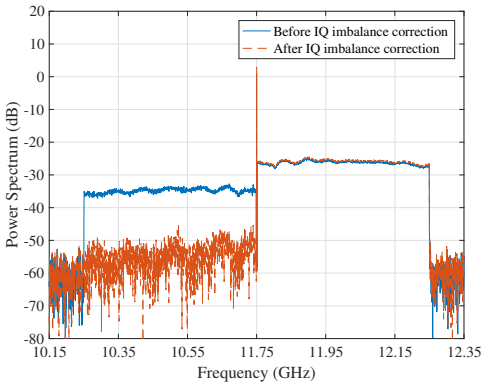

Fig. 6. Sideband suppression before and after IQ imbalance correction, the input of the IQ mixer modified to include only the tones in the upper sideband of the LO. The power observed on the left of LO are due to IQ imbalance.

the TX sounding waveform is digitally pre-distorted according to the obtained phase and amplitude correction values for each sub-band. The RX IQ imbalance correction is performed off-line as described in [38] before further processing. Prior to each measurement campaign, the accuracy of the IQ imbalance correction is validated by checking the sideband suppression ratio with IQ inputs to form a single-sideband modulated signal. Hence for this test, to include only the tones in the upper sideband of the LO, the sounding signal is modified as:

$$m_{\text{USSB}}(t) = \sum_{n=1}^{N} e^{j(n2\pi\Delta f t + \theta_n)} \tag{3}$$

where Δf is the tone spacing, N is the number of tones and θ_n is the phase of the tone n. Again the I and Q signals are real and imaginary parts of $m_{\text{USSB}}(t)$. Fig. 6 shows the spectrum of the received signal with and without IQ imbalance correction for a thru connection. The sideband suppression ratio, which is the ratio of the power in the desired sideband over to the suppressed sideband (in this case ratio of the upper sideband over lower sideband) is only 9 dB before correction, for a carrier frequency of 11.75 GHz (the band with the worst IQ imbalance initially). The applied IQ imbalance correction increases the side-band suppression ratio to more than 25 dB.

B. Stitching Multiple Bands

In this section, we investigate the measurement results for a thru connection to verify the calibration and stitching approach. To achieve a comparable SNR in different sub-bands, the power of the sounding signal and the LO is adjusted per sub-band. The same power levels are used in the calibration measurements as well. Fig. 7(a) shows the measured frequency responses (i.e., $H_{\text{m},k}$) for all sub-bands. The stitching of the multiple bands is based on the fact that the channel does not change during the time it takes to measure two adjacent bands (in the calibration setup, using a cable connection as the channel, there is no change at all, but even for the later measurements of the wireless channel, phase changes due to the Doppler effect occur on a larger time scale than the frequency switching time). Thus, any differences

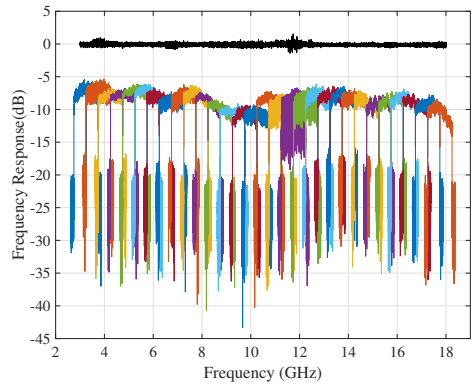

(a) Frequency response

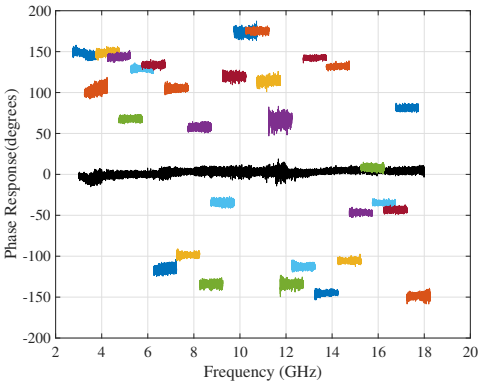

(b) Phase response

Fig. 7. Measured sub-band frequency and phase responses (colored lines) and calibrated/stitched frequency and phase responses (black line)

between the transfer function at the same subcarrier frequency, when measured with two different (overlapping) bands, has to be due to the channel sounder response, which has to be compensated as described in more detail below. Fig. 7(a) also shows the stitched frequency response after calibration and IQ imbalance correction. Even though the overlapping tones in the adjacent sub-bands may look different in the initial measurements, once calibrated they are well aligned within 1 dB, and there are no significant discontinuities in the final frequency response. Hence there is no need for additional correction for the amplitude of the frequency response while stitching adjacent bands.

In case of the phase response; due to the nature of the PLL in the frequency synthesizer, every time the synthesizer switches to a new carrier frequency, it does so with a random phase. Consequently, there is a random phase offset between consecutive sub-band measurements as seen Fig. 7(b). The phase offsets change for every run of a full sweep, hence they need to be estimated and corrected to acquire the true combined phase response for 3 GHz to 18 GHz. The random phase offset from sub-band $k-1$ to sub-band k is calculated with a maximum likelihood estimator which is formulated as follows:

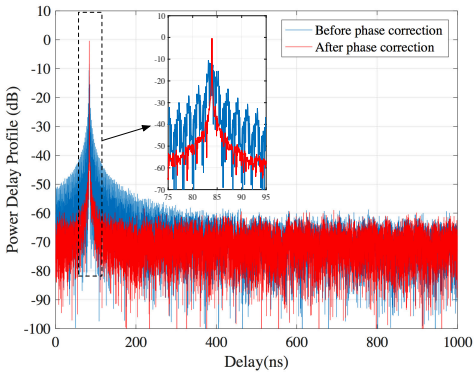

Fig. 8. PDP for the system response with and without phase correction - PDP is shifted on the delay axis for presentation purposes

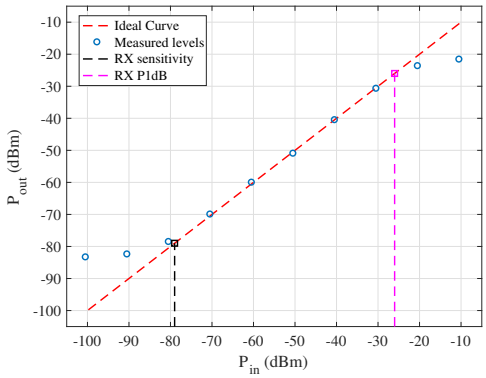

Fig. 9. Dynamic range of the RX, black dashed line indicates the RX sensitivity level, magenta line indicate the RX 1 dB compression point

$$\psi_k = \begin{cases} 0, & \text{for} \quad k = 1 \\ \angle \left(\sum_{f=0}^{f_s} \hat{H}_{k-1}(f) \hat{H}_k^*(f - f_s) \right), & \text{for} \quad 2 \leq k \leq N_{\text{bands}} \end{cases} \tag{4}$$

where $\angle$ denotes the phase of a complex number and N_{bands} is the number sub-bands. Finally, the stitched complex frequency response for all sub-bands is calculated by;

$$H(f_k + f) = \hat{H}_k(f_k + f) exp\left(j \sum_{n=1}^{k} \psi_n \right)$$

$$\begin{aligned} &\text{Where: } 1 \leq k \leq N_{\text{bands}}, \\ &\quad -f_s/2 < f \leq f_s/2, \\ &\quad f_s \text{ is the step size for the carrier frequencies,} \\ &\quad f_k \text{ is the } k\text{-th carrier frequency.} \end{aligned} \tag{5}$$

Fig. 7(b) shows the phase response for the uncalibrated sub-band measurements along with the phase response of the full-sweep after performing calibration, IQ imbalance and phase corrections. Additionally, Fig. 8 shows the power delay profiles (PDPs) for a thru connection with and without phase correction. The phase correction removes the undesired ripples caused by phase jumps in the frequency response. To test the temporal stability of the calibration, we repeated the measurement with the thru connection 100 times; the maximum deviation in power was 0.2 dB. Phase and gain offset corrections are implemented as part of the post-processing scripts and performed automatically for every single measurement point.

IV. System Performance

A. Dynamic Range and Measurable Path Loss

Given the values in Table I, the estimated noise figure for the RX is 5 dB. At any given time, the RX measures a sub-band with 1 GHz bandwidth. The resulting RX sensitivity is:

$$\begin{aligned} RX_{\text{sensitivity}} &= -174 \text{ dBm/Hz} + 5 \text{ dB} + 10 * log_{10}(1e9) \text{ Hz} \\ &= -79 \ dBm \end{aligned} \tag{6}$$

With the 40 dBm transmitting power, the instantaneous measurable path loss for the channel sounder is 119 dB. Since we employ a RX waveform averaging factor of 20 (i.e., sounding waveform is transmitted 20 times for each sub-band), we gain additional 13 dB resulting in a measurable path loss of 132 dB.

Fig. 9 shows the dynamic range of the RX. P_{in} is the input power to the RX RF connector and the P_{out} is the estimated power from the recorded waveform averaged over the whole band. In parallel to the estimated RX sensitivity, noise power distorts the estimated power if the input power is below -79 dBm. For -80 dBm input power, the estimated power is -78.2 dBm. Since the 1 dB compression input power for the RX LNA is -26 dBm, the dynamic range of the RX is 53 dB. Note that during the measurement campaigns for the points with RX power more than -30 dBm, a variable attenuator[1] is placed before the RX LNA to ensure the linearity of the RX. For the points within the dynamic range of the RX, the root mean square error (RMSE) of the estimated power levels with respect to the input power is 0.4 dB.

B. 2-path Coaxial Channel Validation Measurements

In this section, we use a deterministic channel to test the channel sounder. A coaxial 2-path channel was created by using a power divider, delay line and a power combiner. The impulse response of the corresponding analytical channel is $h(\tau) = \alpha_1 e^{j\phi_1} \delta(\tau - \tau_1) + \alpha_2 e^{j\phi_2} \delta(\tau - \tau_2)$, where $\delta(\tau)$ is the Dirac delta function and α_k, ϕ_k and τ_k are respectively the amplitude, phase and delay of the kth path. The values of these parameters are given in Table III.

TABLE III
Parameter values for the 2-path test channel

Path number k	Amplitude α_k	Phase ϕ_k	Delay τ_k
1	0.31	-2.7 radians	25.2 ns
2	0.23	1.2 radians	36.9 ns

Fig. 10(a) compares the frequency response from the analytical channel with the frequency response with the channel

[1]A manual variable attenuator was used for this purpose. The attenuation level is set to a fixed value for each continuous set of measurements (i.e., RX is moving on a line)

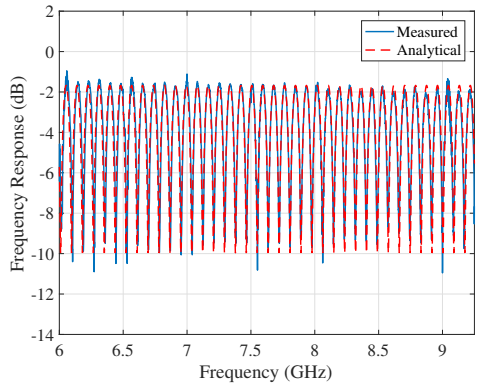

(a) The analytical and the measured frequency responses for the 2-path test channel

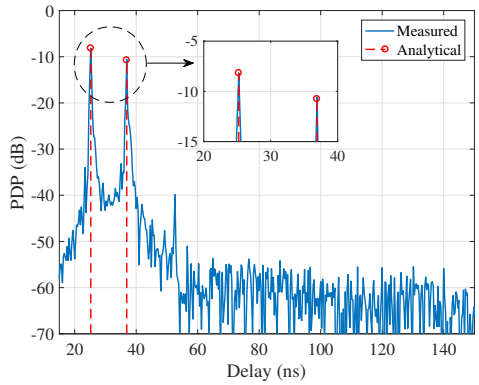

(b) The analytical and the measured PDPs for the 2-path test channel, close-in shows the two paths created by using the coaxial components

Fig. 10. Comparison of the measured 2-path coaxial channel with the analytical channel response

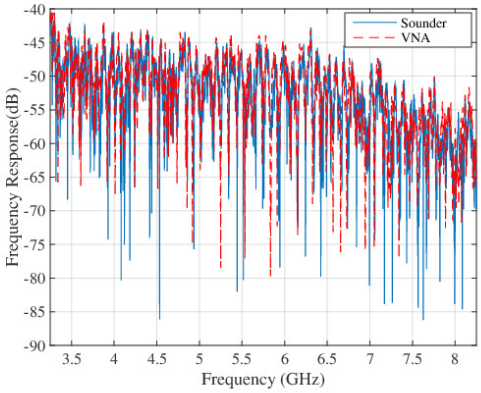

(a) Frequency response

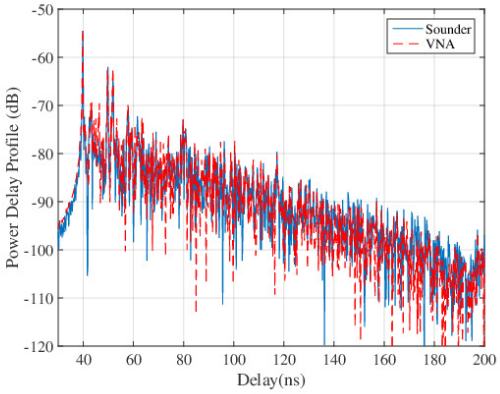

(b) Power delay profiles

Fig. 11. Comparison of the measured frequency responses and power delay profiles for same environment with VNA and the proposed setup

sounder. The RMSE for the measured frequency response with respect to the analytical channel is 0.89 dB. As seen in Fig. 10(b), the estimated errors in the powers of the paths are 0.01 dB for the first path and 0.19 dB for the second path. Furthermore, in the measured PDP, there are additional peaks due to the reflections between the components in the test channel. However, the power of these reflections are more than 30 dB below the paths under investigation.

C. Over The Air (OTA) Validation Measurements

As the final verification, we compared the results from the channel sounder setup with those from a VNA i.e., measurements of the same wireless channel were taken with the channel sounder setup and the VNA. For a sample location, Fig. 11(a) shows the frequency responses obtained from VNA and the calibrated and stitched frequency response acquired with the proposed channel sounder. If we calculate the RMSE in dB-scale similar to the Section IV-B, the RMSE for the frequency response is 4.8 dB. However, this error is mainly dominated by the larger errors caused by not-aligned fading dips (i.e., although measurements are taken in the same environment, slight changes in the TX-RX locations affect the frequency of a fading dip). Additionally, Fig. 11(b) presents the same comparison for power delay profiles. The same specular components can be observed in both responses, and the power of the line-of-sight (LOS) path differs only by 0.1 dB between two cases. The total powers estimated for the two measurement differ by 0.4 dB between two measurements. Consequently, the measurement acquired via the two methods are in good agreement, which validates the proposed channel sounder and calibration procedure.

D. Impact of Antenna Pattern and Multiple Input Multiple Output (MIMO) Extension

As a single input single output (SISO) setup, the channel sounder is only capable of measuring the "radio channel", i.e., the concatenation of the propagation channel with the antennas [39]. The frequency characteristics of that radio channel are thus impacted by the frequency dependence of the antennas as well as that of the propagation. Since we aim to characterize the propagation, the antenna patterns should be as independent of frequency as possible. We stress that a frequency dependence of the antenna gain is not problematic as long as it is the same for all directions, since it can be calibrated out from the overall measurements (as indeed done in our setup). However, if the gain emphasizes some directions at one frequency and others at a different frequency, the results become specific to this particular antenna/channel

combination, and are thus less useful. For this reason, we used bi-conical antennas whose pattern shape is fairly constant over frequency as can be see in Figures 3(a) and 3(b), though some residual impact remains, see also the examples in Ref. [31].

A complete elimination of the impact of the antennas would require measurements with a MIMO channel sounder (also known as double-directional), as this allows to determine the directions of the MPCs at TX and RX. With the proper calibration of the antenna array responses and post-processing, it becomes possible to completely decouple the response of the propagation channel from the response of the antenna arrays [39] by using high-resolution parameter extraction algorithms such as space-alternating generalized expectation-maximization (SAGE) [40] or joint maximum likelihood estimation (RIMAX) [41]. Consequently, the resulting channel characteristics would solely depend on the characteristics of the channel. While the standard RIMAX implementation assumes frequency independence of the antenna patterns (i.e., only applicable to narrowband measurements in which the antenna pattern is not dependent on the frequency), a version of the algorithm extending it to the frequency-dependent (UWB) case is given in Ref. [42] for a single input multiple output (SIMO) case, and generalization to MIMO is relatively straightforward.

Although the channel sounder presented here is a SISO setup, the same principle can be used to build a MIMO channel sounder by employing antenna arrays at the TX and the RX. Extension to a MIMO channel sounder could be achieved by connecting the output of the TX amplifier to an electronic switch that connects the signal sequentially to the different elements of the transmit array (and similarly at the receiver) [43]. However, hardware implementation of such a structure is beyond the scope of this paper. Even with the MIMO extension, the designed channel sounder will still be able to operate in dynamic channels. Since most of the measurement duration is due to the frequency switching delay, the best way to scan all antenna pairs at all frequencies would be measuring all MIMO channels before switching to next carrier frequency. The resulting time spent for recording a MIMO snapshot would be:

$$SweepTime = ((N_T \times N_R \times T_{\text{SISO}}) + T_{\text{switch}}) \times N_{\text{bands}} \quad (7)$$

where N_T and N_R are the number of antennas at the TX and the RX, respectively. T_{SISO} is the time spent for sounding one TX-RX antenna pair, T_{switch} is the buffer time for frequency switching and the N_{bands} is the number of bands to be measure. In our current configurations; we set $T_{\text{SISO}} = 4$ μs, $T_{\text{switch}} = 100$ μs and $N_{\text{bands}} = 30$. If we assume that we extend our current setup to a typical arrangement of such arrays with 8 antenna elements at the TX and the RX, the total time is approximately 10 ms which is five orders of magnitude faster than the state of the art method of combining a VNA with a virtual array [44], and an order of magnitude smaller than what a VNA would require even to measure a SISO channel.

With uniform switching, the maximum measurable Doppler would be $\pm$ 83.33 Hz. However, one can improve the measurement Doppler by using the irregular switching approach

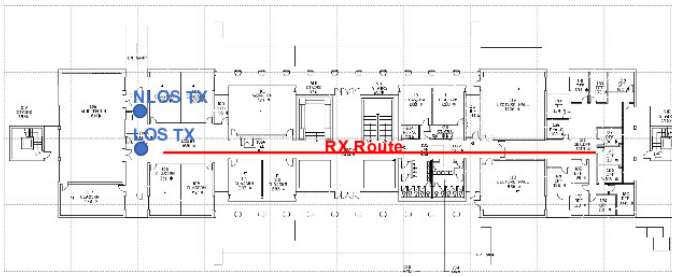

Fig. 12. Floor plan for 1st floor (each grid corresponds to 10m)

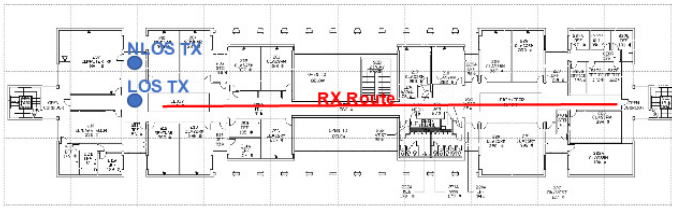

Fig. 13. Floor plan for 2nd floor (each grid corresponds to 10m)

described in [45], [46]. Note that the IQ imbalance, phase discontinuity between adjacent frequency bands and the amplitude pre-distortion would be same for all antenna pairs in the same sub-band, so the post-processing steps would still follow Section III.

V. Measurement Campaign

In this section, we describe the test measurements we performed with the channel sounder to demonstrate both the usefulness of the channel sounder and the validity of operation in a real environment. The measurements were performed in the Grace Ford Salvatori Hall (GFS) on the University of Southern California campus. The measurements were repeated on two different floors, with slightly different floor plans as shown in Figs. 12 and 13. For each floor, there are one LOS and one non-line-of-sight (NLOS) TX locations. For both cases, the TX is stationary while the RX continuously moves on the same line along the corridor, at a speed of $0.2\,\text{m/s}$. Measurements were taken every $1\,\text{s}$ and in each measurement, our setup records five snapshots of the channel impulse response (i.e five frequency sweeps covering $3\,\text{GHz}$ to $18\,\text{GHz}$), with a time gap of $10\,\text{ms}$ between successive snapshots.

Both the TX and the RX antennas are placed at $1.5\,\text{m}$ height, similar to a typical device to device (D2D) scenario. In case of LOS, the TX-RX distances range from $5\,\text{m}$ to $53\,\text{m}$ for the first floor and from $5\,\text{m}$ to $70\,\text{m}$ for the second floor. Similarly, in case of NLOS, the distances range from $9\,\text{m}$ to $55\,\text{m}$ for the first floor and from $9\,\text{m}$ to $73\,\text{m}$ for the second floor. As a manual variable attenuator is used to ensure linearity of the RX, these routes were divided into 2 or 3 sections which are measured with a fixed gain continuously. Each section is measured with different attenuation levels and the values are recorded for post-processing. Since the GPS-based location accuracy deteriorates indoor, we also marked checkpoints on

the measurement route and time the RX movement to ensure a more accurate TX-RX distance determination.

A. Noise Averaging and Interference Filtering

The multiple snapshots acquired within the same burst experience similar small-scale fading, since the maximum distance covered within 40 ms (i.e., maximum time gap between the first and the last snapshot) is less than half a wavelength for all frequencies. Hence these snapshots can be used for noise averaging.

The multiple snapshots can also be used to detect and suppress the bursty 5 GHz WiFi interference, which was observed occasionally. Since the interference might be present only in a subset of the snapshots, using a pair wise correlation of the snapshot channel impulse responses, followed by median filtering, we can discard the snapshots corrupted by interference [11], [31]. The remaining snapshots are used for noise averaging.

B. Averaged Power Delay Profile (APDP) computation

Let $\{H_{\mathrm{T}}(f_k), k = 1 \cdots N_{\mathrm{F}}\}$ be the wideband channel frequency response measured at time T seconds (time is measured relative to the first measurement in that route), where $f_1 = 3$ GHz, $\Delta f = f_2 - f_1 = 0.5$ MHz and $N_{\mathrm{F}} = 30001$. Then the wideband impulse response $h_{\mathrm{T}}(\tau)$ is calculated by taking an inverse fast Fourier Transform (IFFT) with a Hann window to suppress the side lobes. The magnitude squared of the impulse response gives the instantaneous power delay profile, $PDP_{\mathrm{T}}(\tau)$.

Along the route, consecutive measurements were taken 0.2 m apart, which corresponds to 2λ spacing at 3 GHz carrier frequency and 12λ at 18 GHz carrier frequency. Consequently, the successive measurements experience essentially independent small-scale fading. Hence, the effects of the small-scale fading can be removed by averaging successive N PDP measurements, where N is the number of consecutive measurements in which the MPC have similar powers with independent phase realizations. N is characterized by using the correlation between the instantaneous PDPs and the variation in the overall received power. Finally, the APDP is given by

$$APDP(\tau) = \frac{1}{N} \sum_{\mathrm{T}=k}^{k+N-1} PDP_{\mathrm{T}}(\tau) \tag{8}$$

where $N \triangleq \min(N_1, N_2)$. N_1 denotes the number of consecutive measurements over which the PDPs are correlated (i.e., correlation is larger than 0.5 [47]–[49]) and N_2 denotes the number of consecutive measurements whose received power does not vary by more than 3 dB.

$$N_1 = \min\{n : Corr(PDP_k(\tau), PDP_{k+n}(\tau)) < 0.5\} \tag{9}$$

$$N_2 = \min\{n : |P_k - P_{k+n}| > 3\ dB\} \tag{10}$$

where $Corr(.,.)$ denotes the correlation coefficient and $P_{\mathrm{T}} = 10\log_{10}\left(\sum_{k=1}^{N_{\mathrm{F}}} |H_{\mathrm{T}}(f_k)|^2\right)$ denotes the power in the channel frequency response. More details about the post-processing can be found in Ref. [31].

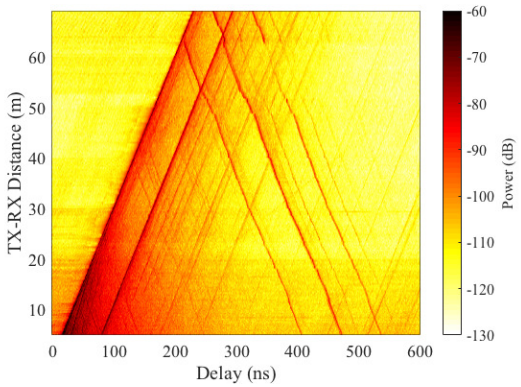

Fig. 14. APDP(dB) vs TX-RX distance for the second flor LOS measurements

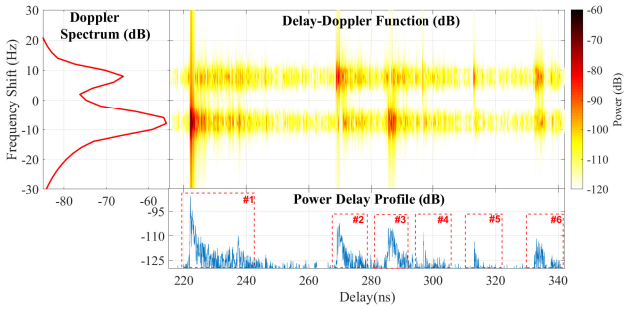

Fig. 15. Spreading (delay-Doppler) function, power delay profile and Doppler spectrum for the same measurement snapshot. Stationary TX and RX is moving away from TX with a speed of 0.2 m/s, TX-RX distance: 66.65 m.

Fig. 14 shows all LOS APDPs measured on the the second floor. The first two MPCs with initial delays of 17 ns and 80 ns correspond to the LOS path and the reflection from wall behind the TX. As the RX moves away from the TX, the delays of these MPCs increase linearly with a slope of corresponding to the speed of the electromagnetic waves (i.e., approximately 3e8 meters per second) as expected. Two other dominant MPCs with initial delays of 405 ns and 470 ns are caused by the reflections from the walls at the end of the corridor. Another MPC with initial delay of 535 ns is caused by the double reflection from the wall behind the TX and the wall at the end of the corridor. Hence the delays of these three MPCs decrease linearly as the RX moves down the corridor.

Next, we demonstrate the channel sounders capability of operating in dynamic environments by investigating the delay-Doppler spreading function[2] observed for a time-varying measurement. Fig. 15 shows the spreading function along with the power delay profile and Doppler spectrum for the same measurement snapshot which corresponds to the TX-RX distance of 66 m in Fig. 14.

During this measurement, the TX is stationary while the RX is moving away from TX with a speed of 0.2 m/s. The dominant clusters are marked on the PDP in Fig. 15; clusters

[2]The spreading function, also known as Doppler variant impulse response, is calculated by taking a Fourier transformation of the impulse responses which respect to time [29].

#1 and #3 are LOS path and the reflection from the wall behind the TX, hence they have positive Doppler. Due to the wide measurement bandwidth, the observed Doppler shifts vary from 2 Hz at 3 GHz to 12 Hz at 18 GHz. All other clusters (i.e #2, #4, #5 and #6) are reflections (single or double) from the end-wall and have the same amount of negative Doppler. Consequently, the Doppler spectrum shown on the left hand-side in Fig. 15 has two peaks at approximately ± 8 Hz. Due to slow movement of the RX, the observed Doppler shifts are relatively small. However, with 15 GHz bandwidth, the channel sounder is capable of measuring channels with Doppler shifts up to ± 83.33 Hz. Larger Doppler shifts (i.e., more dynamic channels) can be measured by sacrificing bandwidth, maximum measurable excess delay or measurement SNR.

C. Delay Spread

In this section, we investigate the omni-directional RMS-DS for the indoor environment and its frequency dependency. The RMS-DS τ_{RMS} is computed as the second central moment of the APDP [29].

$$\tau_{\mathrm{RMS}} = \sqrt{\frac{\int_0^\infty (\tau - \bar{\tau})^2 \, APDP(\tau)\, d\tau}{\int_0^\infty APDP(\tau)\, d\tau}} \tag{11}$$

where $\bar{\tau}$ is the mean delay, which is given by

$$\bar{\tau} = \frac{\int_0^\infty \tau APDP(\tau)\, d\tau}{\int_0^\infty APDP(\tau)\, d\tau} \tag{12}$$

To reduce the effects of noise, we remove the noise power from the APDP, by a noise-thresholding filter, in which the APDP samples whose magnitude are below a threshold are set to zero. The threshold is set to be 6 dB above the noise floor. The noise floor is computed from the noise-only region of the APDP (samples before the first MPC).

Fig. 16(a) shows the LOS RMS-DS with respect to the TX-RX distance. The values we observe vary between 15 ns and 55 ns. For both floors, the RMS-DS increases with distance until 30 m, after which it decreases. After further inspection of the PDPs, we justify this trend with the following observations that are related to the particular geometry of the environment. Initially, the direct path is much stronger than any other paths, resulting in a relatively smaller delay spread, see Fig. 14. As we move along the corridor, the other paths with larger excess delays are getting relatively stronger. Consequently, RMS delay spread slightly increases. Especially, due to its large excess delay, the emergence of the path reflected by the wall at the end of the route is the main contributor to the increase in the RMS DS values. The travel distance for the path reflected by the wall at the end decreases as we move towards that wall. Hence, this path is also getting absolutely stronger as the TX-RX distance increases and causes RMS-DS to increase as well. As we move even closer to this wall the excess delay of the reflected path relative to direct path gets smaller, hence the RMS delay spread gradually decreases again after 30m.

For the NLOS case, the RMS-DS values are within 25 ns to 60 ns except two segments [25 m, 40 m] and [62 m, 67 m] on the second floor as shown in Fig. 16(b). Within these segments,

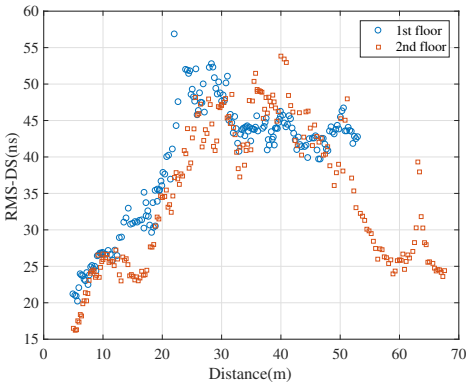

(a) RMS-DS for LOS measurements versus TX-RX distance

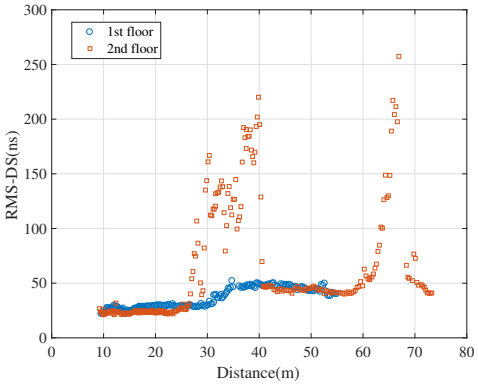

(b) RMS-DS for NLOS measurements versus TX-RX distance, between 26 m and 40 m, 62 m and 70 m, the RMS-DS is significantly higher due to additional paths from outdoor

Fig. 16. Comparison of the measured frequency responses and power delay profiles for same environment with VNA and the proposed setup

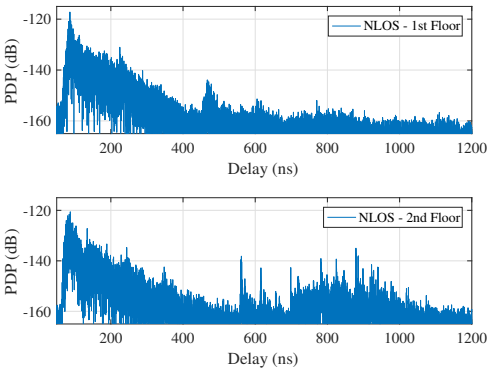

Fig. 17. 1st and 2nd floor NLOS APDP at 35 m, the MPCs with delays more than 500 ns are caused by the reflections from surrounding buildings.

the RMS-DS takes on values as high as 250 ns. When the RX is in one of these segments, both the NLOS TX and the RX have clear views to windows, allowing reflections from surrounding buildings to arrive at the RX. An example APDP for this case in comparison to the first floor is shown in Fig. 17. The MPCs with an excess delay more than 500 ns on the second floor are due to these *external* MPCs. Note that the excess delays for these paths are consistent through-out the

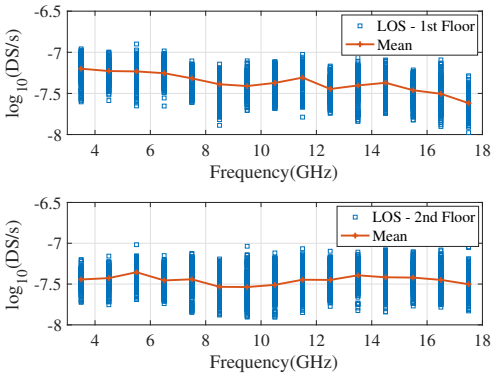

(a) LOS

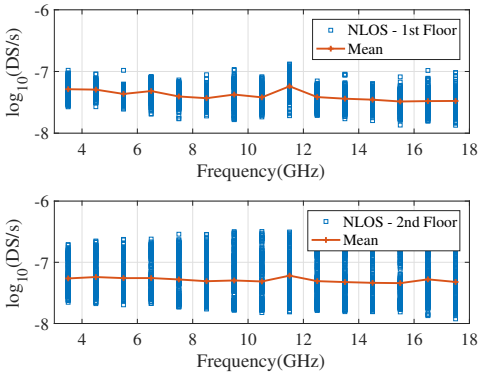

(b) NLOS

Fig. 18. LOS and NLOS RMS-DS in logarithmic scale along with means versus the center frequency of sub-bands

whole segment, and they are observed in all individual sub-bands from 3 GHz to 18 GHz, hence they are indeed MPCs and can not be caused by some kind of interference. Ref. [50] presents omnidirectional RMS-DS values observed in the 13-17 GHz frequency band for two indoor environments. The non-parametric results (i.e., delay spread is calculated from the power delay profile and not from the extracted MPCs which are the output of SAGE algorithm) presented in the paper indicate RMS-DS values ranging from 8 ns to 35 ns. Since the measured TX-RX distances and the measurement environments are relatively smaller than in our case, the observed RMS-DS are also less than what we observed.

Next, we investigate the frequency dependency of the omni-directional RMS-DS by dividing the measured frequency responses into 1 GHz sub-bands and calculating the RMS-DS for each sub-band. Figs. 18(a) and 18(b) show the logarithm of the RMS-DS in seconds for all measurement points versus the center frequency of the sub-band. Following the the proposed model of the 3rd Generation Partnership Project (3GPP) [51], we model the frequency-dependent RMS-DS on a logarithmic scale as follows;

$$\mu_{\log(\mathrm{DS})}(f_c) = \alpha log(1 + f_c) + \beta \tag{13}$$

where $\mu_{\log(\mathrm{DS})}(f_c)$ is the mean of the logarithm of the RMS-DS (in seconds) at the center frequency of f_c in GHz. α and β are the model parameters to be estimated from the measured

TABLE IV
ESTIMATED PARAMETERS FOR THE FREQUENCY DEPENDENT RMS-DS MODEL GIVEN IN EQ. 13

Location	α (%95 confidence interval)	β
LOS-1st Floor	-0.53 (-0.67, -0.39)	-6.82
LOS-2nd Floor	-0.04 (-0.17, 0.09)	-7.41
NLOS-1st Floor	-0.29 (-0.43, -0.16)	-7.09
NLOS-2nd Floor	-0.12 (-0.19, -0.04)	-7.17

data. As seen in Table IV, for all scenarios the $\mu_{\log(\mathrm{DS})}$ decreases with frequency (i.e., α is negative). However, for LOS-2nd Floor data the 95% confidence interval includes positive values for α, indicating the decreasing trend can not be confirmed with 95% confidence level. For the other three measurement scenarios, the RMS-DS decreases with frequency with more than 95% confidence. In [23], similar models for the frequency dependency of the omni-directional RMS-DS in several indoor environments were proposed. The most relevant campaign to our work is the *EAB Office* measurements performed at 2.4 GHz, 5.8 GHz, 14.8 GHz and 58.7 GHz center frequencies. The estimated α's are -0.07 and -0.01 for LOS and NLOS, respectively. However, since the 95% confidence intervals for both cases consist of both negative and positive values for α, the authors do not claim a clear dependency of the RMS-DS on the frequency. Ref. [52] also studies the dependency of the RMS-DS on the frequency by investigating 500 MHz bands centered at 1.25 GHz, 2.25 GHz, 5.25 GHz, 5.75 GHz, and 10.75 GHz. Similarly, they observed a slight negative dependency of the delay spread on the frequency. Parallel to these references, in our observation, the delay spread tends to decrease with frequency, however, the slope of the decrease is very small (even negligible) in almost all cases. This is an important factor which might impact future system design at frequencies beyond 6 GHz. Additional measurements in different indoor environments performed with the presented channel sounder would be instrumental to further investigate the frequency dependency of the RMS-DS.

VI. CONCLUSIONS

In this paper, we presented an UWB real-time channel sounder operating from 3 GHz to 18 GHz. Using a frequency-hopped sub-band approach, the channel sounder can measure the whole band in 6 ms without requiring high-speed digitizers and waveform generators. We discussed calibration and post-processing steps to combine sub-bands into a single 15 GHz band. The achieved RX sensitivity and the dynamic range of the channel sounder are -79 dBm and 53 dB, respectively. The channel sounder operation is tested with a deterministic coaxial channel, the observed RMSE of the estimated frequency response was 0.89 dB. The constructed channel sounder and the post-processing techniques are also validated by comparing the measured impulse response with a VNA measurement. Since the TX and the RX do not require any physical connection, the setup is suitable for both indoor and outdoor channel sounding campaigns. Initial measurement results for indoor environment showed that the wideband RMS-DS varies from 15 ns to 55 ns for LOS, and 30 ns to

250 ns for NLOS measurements. Additionally, using 1 GHz sub-bands of the frequency response, we investigated the frequency dependency of the RMS-DS. We observed that the RMS-DS decreases with the frequency in all scenarios, and the trend is statistically significant for three out of four measurement scenarios, however, the slope of the decrease is very small for all cases. In the future, the channel sounder will be used to investigate the dependencies of the path loss exponents, shadow fading, RMS-DS, Ricean factor and coherence bandwidth on the frequency in the 3-18 GHz band for other environments. We also discussed the fundamental possibilities of extending the measurement principle to MIMO channel sounders.

ACKNOWLEDGEMENT

The authors would like to thank Northrop Grumman for providing antennas and amplifiers during initial tests.

REFERENCES

[1] C. U. Bas, V. Kristem, R. Wang, and A. F. Molisch, "Real-time ultra-wideband frequency sweeping channel sounder for 3-18 GHz," in *IEEE Military Communications Conference (MILCOM)*, October 2017, pp. 775–781.

[2] J. Gozalvez, "Mobile traffic expected to grow more than 30-fold [mobile radio]," *IEEE Vehicular Technology Magazine*, vol. 6, no. 3, pp. 9–15, September 2011.

[3] T. S. Rappaport, S. Sun, R. Mayzus, H. Zhao, Y. Azar, K. Wang, G. N. Wong, J. K. Schulz, M. Samimi, and F. Gutierrez, "Millimeter wave mobile communications for 5G cellular: It will work!" *Access, IEEE*, vol. 1, pp. 335–349, 2013.

[4] A. F. Molisch, A. Karttunen, R. Wang, C. U. Bas, S. Hur, J. Park, and J. Zhang, "Millimeter-wave channels in urban environments," in *2016 10th European Conference on Antennas and Propagation (EuCAP)*, April 2016, pp. 1–5.

[5] K. Haneda, "Channel models and beamforming at millimeter-wave frequency bands," *IEICE Transactions on Communications*, vol. 98, no. 5, pp. 755–772, 2015.

[6] J. Gozalvez, "Prestandard 5G developments [mobile radio]," *IEEE Vehicular Technology Magazine*, vol. 9, no. 4, pp. 14–28, December 2014.

[7] D. Cox, "910 MHz urban mobile radio propagation: Multipath characteristics in New York City," *IEEE Transactions on Communications*, vol. 21, no. 11, pp. 1188–1194, November 1973.

[8] V. Erceg, L. J. Greenstein, S. Y. Tjandra, S. R. Parkoff, A. Gupta, B. Kulic, A. A. Julius, and R. Bianchi, "An empirically based path loss model for wireless channels in suburban environments," *IEEE Journal on Selected Areas in Communications*, vol. 17, no. 7, pp. 1205–1211, July 1999.

[9] M. Toeltsch, J. Laurila, K. Kalliola, A. F. Molisch, P. Vainikainen, and E. Bonek, "Statistical characterization of urban spatial radio channels," *IEEE Journal on Selected Areas in Communications*, vol. 20, no. 3, pp. 539–549, April 2002.

[10] Z. Sun and I. F. Akyildiz, "Channel modeling and analysis for wireless networks in underground mines and road tunnels," *IEEE Transactions on Communications*, vol. 58, no. 6, pp. 1758–1768, June 2010.

[11] V. Kristem, S. Sangodoyin, C. U. Bas, M. Kaeske, J. Lee, C. Schneider, G. Sommerkorn, C. J. Zhang, R. S. Thomae, and A. F. Molisch, "3D MIMO outdoor-to-indoor propagation channel measurement," *IEEE Transactions on Wireless Communications*, vol. 16, no. 7, pp. 4600–4613, July 2017.

[12] S. Ranvier, J. Kivinen, and P. Vainikainen, "Millimeter-wave MIMO radio channel sounder," *IEEE Transactions on Instrumentation and Measurement*, vol. 56, no. 3, pp. 1018–1024, June 2007.

[13] W. Fu, J. Hu, and S. Zhang, "Frequency-domain measurement of 60 GHz indoor channels: a measurement setup, literature data, and analysis," *IEEE Instrumentation Measurement Magazine*, vol. 16, no. 2, pp. 34–40, April 2013.

[14] T. Rappaport, G. Maccartney, M. Samimi, and S. Sun, "Wideband millimeter-wave propagation measurements and channel models for future wireless communication system design," *Communications, IEEE Transactions on*, vol. 63, no. 9, pp. 3029–3056, September 2015.

[15] P. B. Papazian, C. Gentile, K. A. Remley, J. Senic, and N. Golmie, "A radio channel sounder for mobile millimeter-wave communications: System implementation and measurement assessment," *IEEE Transactions on Microwave Theory and Techniques*, vol. 64, no. 9, pp. 2924–2932, September 2016.

[16] S. Salous, S. M. Feeney, X. Raimundo, and A. A. Cheema, "Wideband MIMO channel sounder for radio measurements in the 60 GHz band," *IEEE Transactions on Wireless Communications*, vol. 15, no. 4, pp. 2825–2832, April 2016.

[17] G. R. MacCartney and T. S. Rappaport, "A flexible millimeter-wave channel sounder with absolute timing," *IEEE Journal on Selected Areas in Communications*, vol. 35, no. 6, pp. 1402–1418, June 2017.

[18] C. U. Bas, R. Wang, D. Psychoudakis, T. Henige, R. Monroe, J. Park, J. Zhang, and A. F. Molisch, "A real-time millimeter-wave phased array MIMO channel sounder," in *Vehicular Technology Conference, 2017. VTC 2017-Fall. IEEE*, September 2017, pp. 1–6.

[19] R. Müller, S. Häfner, D. Dupleich, R. S. Thomä, G. Steinböck, J. Luo, E. Schulz, X. Lu, and G. Wang, "Simultaneous multi-band channel sounding at mm-Wave frequencies," in *2016 10th European Conference on Antennas and Propagation (EuCAP)*, April 2016, pp. 1–5.

[20] W. Fan, I. Carton, and G. F. Pedersen, "Comparative study of centimetric and millimetric propagation channels in indoor environments," in *2016 10th European Conference on Antennas and Propagation (EuCAP)*, April 2016, pp. 1–5.

[21] W. Fan, I. Carton, J. Ø. Nielsen, K. Olesen, and G. F. Pedersen, "Measured wideband characteristics of indoor channels at centimetric and millimetric bands," *EURASIP Journal on Wireless Communications and Networking*, vol. 2016, no. 1, p. 58, Feb 2016. [Online]. Available: https://doi.org/10.1186/s13638-016-0548-x

[22] J. Huang, C. Wang, R. Feng, J. Sun, W. Zhang, and Y. Yang, "Multi-Frequency mmWave massive MIMO channel measurements and characterization for 5G wireless communication systems," *IEEE Journal on Selected Areas in Communications*, vol. 35, no. 7, pp. 1591–1605, July 2017.

[23] S. L. Nguyen, J. Medbo, M. Peter, A. Karttunen, K. Haneda, A. Bamba, R. D'Errico, N. Iqbal, C. Diakhate, and J.-M. Conrat, "On the frequency dependency of radio channel's delay spread: Analyses and findings from mmMAGIC multi-frequency channel sounding," *arXiv preprint arXiv:1712.09435*, 2017.

[24] A. M. Al-Samman, T. A. Rahman, M. H. Azmi, M. N. Hindia, I. Khan, and E. Hanafi, "Statistical modelling and characterization of experimental mm-Wave indoor channels for future 5G wireless communication networks," *PLOS ONE*, vol. 11, no. 9, pp. 1–29, September 2016. [Online]. Available: https://doi.org/10.1371/journal.pone.0163034

[25] A. F. Molisch, "Ultra-Wide-Band propagation channels," *Proceedings of the IEEE*, vol. 97, no. 2, pp. 353–371, February 2009.

[26] P. Pagani, F. T. Talom, P. Pajusco, and B. Uguen, *Ultra wide band radio propagation channel*. John Wiley & Sons, 2013.

[27] C. U. Bas and S. C. Ergen, "Ultra-wideband channel model for intra-vehicular wireless sensor networks beneath the chassis: From statistical model to simulations," *IEEE Transactions on Vehicular Technology*, vol. 62, no. 1, pp. 14–25, January 2013.

[28] A. Dezfooliyan and A. M. Weiner, "Evaluation of time domain propagation measurements of UWB systems using spread spectrum channel sounding," *IEEE Transactions on Antennas and Propagation*, vol. 60, no. 10, pp. 4855–4865, October 2012.

[29] A. F. Molisch, *Wireless communications*, 2nd ed. IEEE Press - Wiley, 2010.

[30] V. Kristem, C. U. Bas, R. Wang, and A. F. Molisch, "Outdoor macro-cellular channel measurements and modeling in the 3-18 GHz band," in *2017 IEEE Globecom Workshops (GC Wkshps)*, December 2017, pp. 1–7.

[31] V. Kristem, C. U. Bas, R. Wang, and A. F. Molisch, "Outdoor wideband channel measurements and modeling in the 3-18 GHz band," *IEEE Transactions on Wireless Communications*, vol. 17, no. 7, pp. 4620–4633, July 2018.

[32] T. Zwick, T. J. Beukema, and H. Nam, "Wideband channel sounder with measurements and model for the 60 GHz indoor radio channel," *IEEE Transactions on Vehicular Technology*, vol. 54, no. 4, pp. 1266–1277, July 2005.

[33] M.-S. Choi, G. Grosskopf, and D. Rohde, "A novel wideband space-time channel measurement method at 60 GHz," in *2005 IEEE 16th*

International Symposium on Personal, Indoor and Mobile Radio Communications, vol. 1, September 2005, pp. 584–588.

[34] J. li, Y. Zhao, C. Tao, and B. Ai, "System design and calibration for wideband channel wounding with multiple frequency bands," *IEEE Access*, vol. 5, pp. 781–793, January 2017.

[35] M. Friese, "Multitone signals with low crest factor," *IEEE Transactions on Communications*, vol. 45, no. 10, pp. 1338–1344, October 1997.

[36] P. Almers, S. Wyne, F. Tufvesson, and A. F. Molisch, "Effect of random walk phase noise on mimo measurements," in *2005 IEEE 61st Vehicular Technology Conference*, vol. 1, May 2005, pp. 141–145 Vol. 1.

[37] Tektronix, *Application note: Baseband Response Characterization of I-Q Modulators*, February 2014, no. 37W-29553-1.

[38] R. Zetik, M. Kmec, J. Sachs, and R. S. Thomä, "Real-time MIMO channel sounder for emulation of distributed ultrawideband systems," *International Journal of Antennas and Propagation*, September 2014.

[39] M. Steinbauer, A. F. Molisch, and E. Bonek, "The double-directional radio channel," *Antennas and Propagation Magazine, IEEE*, vol. 43, no. 4, pp. 51–63, 2001.

[40] B. H. Fleury, M. Tschudin, R. Heddergott, D. Dahlhaus, and K. I. Pedersen, "Channel parameter estimation in mobile radio environments using the SAGE algorithm," *IEEE Journal on selected areas in communications*, vol. 17, no. 3, pp. 434–450, March 1999.

[41] A. Richter, "Estimation of radio channel parameters: Models and algorithms," Ph.D. dissertation, Techn. Univ. Ilmenau, Ilmenau, Germany, May 2005. [Online]. Available: http://www.db-thueringen.de.

[42] J. Salmi and A. F. Molisch, "Propagation parameter estimation, modeling and measurements for ultrawideband MIMO radar," *IEEE Transactions on Antennas and Propagation*, vol. 59, no. 11, pp. 4257–4267, November 2011.

[43] R. S. Thoma, D. Hampicke, A. Richter, G. Sommerkorn, A. Schneider, U. Trautwein, and W. Wirnitzer, "Identification of time-variant directional mobile radio channels," *IEEE Transactions on Instrumentation and Measurement*, vol. 49, no. 2, pp. 357–364, April 2000.

[44] S. Sangodoyin, V. Kristem, A. F. Molisch, R. He, F. Tufvesson, and H. M. Behairy, "Statistical modeling of ultrawideband mimo propagation channel in a warehouse environment," *IEEE Transactions on Antennas and Propagation*, vol. 64, no. 9, pp. 4049–4063, September 2016.

[45] R. Wang, O. Renaudin, C. U. Bas, S. Sangodoyin, and A. F. Molisch, "Antenna switching sequence design for channel sounding in a fast time-varying channel," in *International Conference on Communications*. IEEE, 2018 (accepted).

[46] R. Wang, O. Renaudin, C. U. Bas, S. Sangodoyin, and A. F. Molisch, "On channel sounding with switched arrays in fast time-varying channels," *arXiv preprint arXiv:1805.08069*, 2018.

[47] K. Guan, B. Ai, Z. Zhong, C. F. Lpez, L. Zhang, C. Briso-Rodrguez, A. Hrovat, B. Zhang, R. He, and T. Tang, "Measurements and analysis of large-scale fading characteristics in curved subway tunnels at 920 MHz, 2400 MHz, and 5705 MHz," *IEEE Transactions on Intelligent Transportation Systems*, vol. 16, no. 5, pp. 2393–2405, October 2015.

[48] 3GPP, "Spatial channel model for multiple input multiple output (MIMO) simulations,," *3GPP TR 25.996 version 6.1.0 Release 15*, September 2003.

[49] G. Senarath, "Multi-hop relay system evaluation methodology (channel model and performance metric)," *http://ieee802.org/16/relay/docs/80216j-06_013r3. pdf*, September 2007.

[50] C. Ling, X. Yin, H. Wang, and R. S. Thomä, "Experimental characterization and multipath cluster modeling for 13-17 GHz indoor propagation channels," *IEEE Transactions on Antennas and Propagation*, vol. 65, no. 12, pp. 6549–6561, December 2017.

[51] 3GPP, "5G; Study on channel model for frequencies from 0.5 to 100 GHz," *3GPP TR 38.901 version 14.3.0 Release 14*, January 2018.

[52] T. Jamsa, V. Hovinen, A. Karjalainen, and J. Iinatti, "Frequency dependency of delay spread and path loss in indoor ultra-wideband channels," in *2006 IET Seminar on Ultra Wideband Systems, Technologies and Applications*, April 2006, pp. 254–258.